Highly conductive, stretchable and biocompatible Ag–Au core–sheath nanowire composite for wearable and implantable bioelectronics

Citation
Choi, Suji, Sang Ihn Han, Dongjun Jung, Hye Jin Hwang, Chaehong Lim, Soochan Bae, Ok Kyu Park et al. "Highly conductive, stretchable and biocompatible Ag–Au core–sheath nanowire composite for wearable and implantable bioelectronics." Nature Nanotechnology 13, no. 11 (2018): 1048-1056. DOI: 10.1038/s41565-018-0226-8

Published Version
doi:10.1038/s41565-018-0226-8

Highly conductive, stretchable, and biocompatible Ag-Au core-sheath nanowire composite for wearable and implantable bioelectronics

Suji Choi[1,2,⊥], Sang Ihn Han[1,2,⊥], Dongjun Jung[1,2,⊥], Hye Jin Hwang[3,⊥], Chaehong Lim[1,2], Soochan Bae[3], Ok Kyu Park[1,2], Cory M. Tschabrunn[3], Mincheol Lee[1,2], Sun Youn Bae[3], Ji Woong Yu[2], Ji Ho Ryu[2], Sang-Woo Lee[4], Kyungpyo Park[4], Peter M. Kang[3], Won Bo Lee[2], Reza Nezafat[3], Taeghwan Hyeon[1,2,]*, and Dae-Hyeong Kim[1,2,]*

[1]*Center for Nanoparticle Research, Institute for Basic Science (IBS), Seoul 08826, Republic of Korea*

[2]*School of Chemical and Biological Engineering, Institute of Chemical Processes, Seoul National University, Seoul 08826, Republic of Korea*

[3]*Cardiovascular Division, Beth Israel Deaconess Medical Center, Harvard Medical School, Boston, MA 02215, USA*

[4]*Department of Physiology, School of Dentistry, Seoul National University, Seoul 03080, Republic of Korea*

⊥ These authors contributed equally to this work.

*To whom correspondences should be addressed.

E-mail: *dkim98@snu.ac.kr and thyeon@snu.ac.kr*

Abstract

Wearable and implantable devices require conductive, stretchable, and biocompatible materials. However, obtaining composites that simultaneously fulfil these requirements is challenging due to a trade-off between conductivity and stretchability. Here we report on Ag-Au nanocomposites composed of ultralong gold-coated silver nanowires in an elastomeric block-copolymer matrix. Owing to the high aspect ratio and percolation network of the Ag-Au nanowires, the nanocomposites exhibit an optimized conductivity of 41,850 S/cm (max: 72,600 S/cm). Phase separation in the Ag-Au nanocomposite during the solvent drying process generates a microstructure that yields an optimized stretchability of 266% (max: 840%). The thick gold sheath deposited on the silver nanowire surface prevents oxidation and silver ion leaching, making the composite biocompatible and highly conductive. Using the nanocomposite, we successfully fabricate wearable and implantable soft bioelectronic devices that can be conformally integrated with human skin and swine heart for continuous electrophysiological recording, and electrical and thermal stimulation.

Conductive and stretchable nanocomposites based on the percolation network of conductive nanomaterials in elastomeric media[1-3] offer a viable alternative to rigid and brittle conventional metallic materials such as gold[4,5] and indium tin oxide[6]. These nanocomposites have been applied in e-skin[7,8], wearable bioelectronics[9,10], and implantable biomedical devices[11,12]. Ultralong one-dimensional metal nanowires are favourable filler materials for these conductive nanocomposites because their high aspect ratio lowers the percolation threshold of filler materials, resulting in high conductivity[13]. Silver (Ag) nanowires are particularly popular because they are highly conductive and can be easily produced on a large scale[13,14]. However, direct exposure of human tissues to Ag ions that leach out from Ag nanowires can have potential adverse health effects[15]. Due to the high oxidation tendency of Ag, Ag nanowires are highly corrosive in biological environments, limiting their applications in bioelectronics[16]. Although gold nanowires have advantages over Ag nanowires in terms of biocompatiblity and oxidation tendency, their conductivity is lower than Ag nanowires, and producing long and thick gold nanowires in large quantity is very challenging[17,18].

Here, we present the highly conductive, biocompatible, and soft Ag-Au nanocomposites consisting of ultralong gold-coated Ag nanowires dispersed in poly(styrene-butadiene-styrene) (SBS) elastomer. The high aspect ratio of Ag nanowires confers high conductivity while the inert gold shell ensures that the nanowires are biocompatible and resistant to oxidation. The phase separation during the low temperature drying process induces microstructures in the nanocomposite, which increases the softness of the material. Cytotoxicity test and histological analysis confirm that the Au sheath effectively improves biocompatibility by preventing Ag ion leaching and protecting Ag nanowires from oxidation. Using the highly conductive, biocompatible, and soft nanocomposites, we successfully fabricated wearable and implantable bioelectronic devices for biosensing and stimulation on the human skin and swine heart.

Fabrication and characterization of the Ag-Au nanocomposite

The fabrication of the microstructured Ag-Au nanocomposite requires a mixture of Ag-Au nanowires decorated with hexylamine ligands, SBS elastomer, and an additional hexylamine in toluene (Fig. 1a). To obtain Ag-Au nanowires, we firstly synthesized ultralong Ag nanowires (~100 μm) using the previous method with slight modifications (Supplementary Fig. 1a)[19,20]. For galvanic-free deposition of Au on the Ag nanowires, we used sodium sulfite to selectively bind Au cations and consequently lower the reduction potential of Au (E^o = 0.111 V vs. standard hydrogen electrode; Supplementary Fig. 1b)[21]. Because the resulting gold(I) sulfite complex is relatively benign to the Ag surface, ligand-assisted oxidative etching does not occur, instead Au coating is boosted. The galvanic replacement reaction is also prevented by keeping the reaction solution at pH 9 (Supplementary Fig. 2)[22]. After the gold coating, the surface of Ag-Au nanowires is modified with hexylamine using the previously-reported ligand exchange procedure (Supplementary Fig. 1c)[23].

To obtain the microstructured Ag-Au nanocomposite, hexylamine-decorated Ag-Au nanowires, a SBS solution, and additional hexylamine in toluene are combined and casted on a glass mold under ambient conditions (Fig. 1b). During the dry-casting and solvent-drying process, the initially homogeneous solution (Fig. 1c left) is separated into two phases, a hexylamine-rich region containing Ag-Au nanowires and a toluene-rich region containing SBS (Fig. 1c middle). Subsequent solvent evaporation results in a microstructured Ag-Au nanocomposite composed of a Ag-Au nanowire-rich region and a SBS-rich region (Fig. 1c right). When the microstructured Ag-Au nanocomposite is stretched, the Ag-Au nanowire rich region maintains the stable electrical conduction and the SBS-rich region forms an elastic microstructured strut (Fig. 1d). Despite the high concentration of the nanowire filler added to the nanocomposite for improved conductivity (Supplementary Fig. 3a), the cushy microstructure ensures softness and stretchability (Fig. 1e, Supplementary Fig. 3b). Stretchability can be further improved by heat rolling-press (Fig. 1f, Supplementary Fig. 3c, Supplementary Movie 1).

We confirmed the Ag-Au nanowire core-sheath structure using various electron microscopy and spectroscopy methods. Scanning electron microscopy (SEM) image in Fig. 2a shows the nanowires are long (~100 μm) and interconnected each other. A backscattered electron image in the inset illustrates the Ag nanowire core and Au sheath (highlighted in yellow) of the Ag-Au nanowire (before surface modification). High-resolution transmission electron microscopy (HRTEM) image of the Ag-Au nanowire shows a clear boundary between the heavy atomic shell (Au) and the light core (Ag) (Fig. 2b). The lattice parameter of the outer shell confirms the crystalline structure of Au in the [111] direction (Fig. 2b inset). Mapping the spatial distribution of Ag and Au using high-angle annular dark field scanning transmission electron microscopy (HAADF-STEM) and energy-dispersive X-ray spectroscopy (EDS) further confirmed the core-sheath structure of the Ag-Au nanowires (Fig. 2c). The smooth morphology indicates that Ag etching by galvanic replacement reaction does not occur. The atomic intensity profile in a line scan of the Ag-Au nanowire (Fig. 2d top) shows that the mean diameter of the nanowire and thickness of the Au shell are 140 nm and 35 nm, respectively (Fig. 2d bottom).

Because oxidation and/or corrosion can increase contact resistance between nanowires, and Ag nanowires are vulnerable to these processes when exposed to biofluids such as sweat[24], interstitial fluid[25], and blood[11], we examined the oxidation resistance of our Ag-Au nanowire using hydrogen peroxide as the oxidant. TEM images show that the Ag nanowire is heavily oxidized and corroded, while the Ag-Au nanowire with the protective Au shell remains intact (Fig. 2e). The resistance against oxidation is further confirmed by UV-Vis spectra, which show a significantly diminished extinction spectrum for Ag nanowires that have undergone oxidation and an unchanged spectrum for Ag-Au nanowires (Fig. 2f). Similar protective effect by the Au shell could be obtained when tested with the Ag-Au nanowires kept in H_2O for 6 months, indicating that the Au shell remains intact for long period of time under the aqueous solution (Supplementary Fig. 4a).

We characterized the conductivity of the Ag-Au nanocomposite (prepared at a 60:40 weight ratio of nanowire:SBS; Fig. 2g). Nanocomposites with longer nanowires (~100 μm) have a higher conductivity (~41,850 S/cm) than those with shorter nanowires (25 μm) (Fig. 2g). The high aspect ratio of the ultralong nanowires significantly reduces their percolation threshold in the nanocomposite compared to zero-dimensional nanoparticles[1] or two-dimensional nanoplates[9]. The percolation threshold of the Ag-Au nanocomposite (V_c = 0.0037; critical volume fraction at a percolation threshold; Supplementary Fig. 5a) is obtained by experiments, which is higher than theoretical percolation threshold ($V_{c,ideal}$ = 0.0009) based on the assumption of ideal distribution of nanowires. This is due to the phase separation effect (Supplementary Fig. 5b)[26]. We also confirmed that the percolation threshold increases in proportional to the applied strain (Supplementary Fig. 5a)[27]. Conductivity can be increased up to around 72,600 S/cm by increasing the content of Ag-Au nanowires in the composite (75:25 weight ratio of nanowires:SBS; Fig. 2h). However, at such a high nanowire content, stretchability decreases. The conductivity of ~41,850 S/cm is obtained at the 60:40 weight ratio of nanowires:SBS, which is the mixing ratio for co-optimization of conductivity and stretchability. In air and physiological solutions, the conductivity of Ag-Au nanocomposite did not deteriorate, while that of the Ag nanocomposite (made of Ag nanowires and SBS) continuously decreased over 3 weeks (Supplementary Fig. 4b and c). For the further confirmation of stability of the Ag-Au nanocomposite, we treated ultraviolet/ozone (UV/O_3) (40 mW/cm^2, 2 hours; ozone as an oxidant) to the nanocomposites. The conductivity of Ag-Au nanocomposite remained unchanged, whereas the conductivity of control Ag nanocomposites deteriorated significantly due to oxidation (Fig. 2i). SEM images confirm severe oxidation of the Ag nanocomposite by UV/O_3 (Fig. 2j top) and the inertness of the Ag-Au nanocomposite (Fig. 2j bottom).

Phase separation effects on the nanocomposite properties

Phase separation determined by solvent drying temperature and hexylamine concentration has a pronounced effect on the conductivity, softness, and stretchability of the Ag-Au nanocomposite. We found that the room temperature solvent drying process leads to a thinner nanocomposite film with a higher density of the percolated nanowire network, and a more conductive nanocomposite than higher temperature processes (Supplementary Fig. 6a and 6b). Room temperature drying facilitates the separation of Ag-Au nanowires into hexylamine-rich regions and promotes the stabilization of SBS in toluene-rich regions (Supplementary Fig. 6c). This phase separation results in the formation of microstructures and regions showing different elasticity (Fig. 3a left, Supplementary Fig. 6d). Upon stretching, a porous microstructure is observed (Fig. 3a right, Supplementary Fig. 7). This cushion-like microstructure lowers Young's modulus and increases softness (Fig. 3b). Computer simulation shows that local stress is distributed in the elastic SBS-rich region under stretching, while the mesh-like Ag-Au nanowire-rich region maintains the original percolation network (Supplementary Fig. 8; see Supplementary Materials and Methods 1.5 for simulation details). For experimental confirmation, we prepared the double-layered Ag-Au nanocomposite encapsulated in elastic substrates (VHB film), and the resistance was measured under stretching. Consequently, the microstructured Ag-Au nanocomposite (0.36:0.24:0.4; weight fraction of Ag-Au nanowires:SBS:hexylamine) fabricated at room temperature shows a conductivity of 41,850 S/cm (at 0% strain) and a stretchability of ~266%, both of which are higher than the composites obtained through the high temperature processes (Fig. 3c).

Another key factor that affects phase separation is the amount of hexylamine. Without hexylamine (*i.e.*, 0 wt% hexylamine), phase separation is limited and no microstructure is formed (Fig. 3d), leading to low stretchability. However, higher weight fraction of hexylamine tends to promote phase separation, and therefore, boosts softness (Fig. 3e) and stretchability (Fig. 3f). When the weight fraction of hexylamine is increased up to 0.4 at the fixed weight ratio of 60:40 for Ag-Au nanowires:SBS, Young's modulus decreases significantly while softness and stretchability increases. Based on our experimental results (22 conditions; n = 3) using different weight fractions of Ag-Au nanowires, SBS, and hexylamine for nanocomposites made under room temperature, we made maps of conductivity and stretchability (Fig. 3g and 3h). The optimum composition to maximize stretchability, while maintaining a high conductivity of 41,850 S/cm is 0.36:0.24:0.4 weight fraction of Ag-Au nanowires:SBS:hexylamine (mapped as red dotted lines in Fig. 3h).

In order to improve stretchability, we increased toughness of the Ag-Au nanocomposite using the heat rolling-press process (Supplementary Fig. 9a, see Methods for details of the heat rolling-press process)[28]. The elastic SBS-rich microstructured struts were cross-linked to each other, and therefore toughness of the Ag-Au nanocomposite increased (Supplementary Fig. 9b). However, the heat rolling-press did not affect the microstructure of the nanocomposite formed by the phase separation (Supplementary Fig. 9c). The stretchability of the Ag-Au nanocomposite (fixed weight ratio of 60:40 for Ag-Au nanowires:SBS) can be increased up to ~840%, when the weight fraction of hexylamine is increased up to 0.3 and the heat rolling-press is applied (Fig. 3i). At the early stage of stretching (*e.g.*, applied strain of 100% or lower), the applied strain is mostly dissipated in the soft SBS rich regions, and therefore electrical conduction in the Ag-Au nanowire rich region is stabilized (Supplementary Fig. 9d and e). As the strain is applied further (*e.g.*, applied strain of 300% or higher), the induced strain in the hard Ag-Au nanowire rich region results in formation of local cracks. But connected electrical pathways via adjacent Ag-Au nanowire rich regions (Supplementary Fig. 9f) as well as Ag-Au nanowires aligned in the stretching direction between the isolated Ag-Au nanowire rich regions (Supplementary Fig. 9g and its inset)[29] stably preserve the percolation network. Meanwhile, when the strain above the critical limit (*e.g.*, applied strain of 840% or higher) is applied, massive charging in SEM occurs, which implies that the percolation of nanowires and electrical pathways through Ag-Au nanowire rich regions become disconnected (Supplementary Fig. 9h). When the weight fraction of hexylamine is 0.3, the roll-pressed Ag-Au nanocomposites exhibit stretchability of 840%, 520%, 300%, and 180% with the initial conductivity of 30,000 S/cm, 38,800 S/cm, 50,600 S/cm, and 69,400 S/cm for 60:40, 65:35, 70:30, and 75:25 Ag-Au nanowire:SBS weight ratios, respectively (Fig. 3j and inset). Electrical and mechanical stability of the Ag-Au nanocomposite after the cyclic stretching test was shown in Supplementary Fig. 10. Even after the Ag-Au nanocomposite with the Ag-Au nanowires:SBS:hexylamine weight fraction of 0.36:0.24:0.4 was stretched with the 10%, 20%, and 30% applied strain repetitively over 3,000 times, there was no significant change in the performance.

Biocompatibility of Ag-Au nanowire composite

For bioelectronic applications, biocompatibility is crucial and preventing direct exposure of Ag nanowires to tissues is important. We examined the effect of the Au sheath on the biocompatibility *in vitro* and *in vivo*. To test the leaching of Ag ions, Ag nanowires, Ag-Au nanowires, and Ag-Au nanocomposite were incubated in Dulbelcco modified eagle medium (DMEM) for 3 days and the dissolution of Ag ions was analysed using inductively coupled plasma mass spectrometry (ICP-MS). DMEM extract for Ag nanowires has 5,349 ppb Ag ions. Very low concentration of Ag ions (311 ppb) was detected in the DMEM extract for Ag-Au nanowires and only trace levels (65 ppb) were detected for the Ag-Au nanocomposite, indicating that the Au sheath effectively inhibits the dissolution of Ag ions (Fig. 4a). The detected Au ion concentration was negligibly low (0.847 ppb; Supplementary Fig. 11). Heart myoblast (H9C2; Fig. 4b) and human skin fibroblast (CCD-986sk; Supplementary Fig. 12) cells exposed to DMEM extract from Ag nanowires showed damaged actin skeleton and DNA while those exposed to extract from Ag-Au nanowires and Ag-Au nanocomposite remained healthy. Furthermore, H9C2, CCD-986sk, and mouse connective tissue (L929) cells exposed to DMEM extracts from Ag nanowires exhibit significantly decreased viability (Fig. 4c). These results confirm that the Au sheath effectively protects the Ag nanowires from leaching potentially lethal Ag ions.

We further implanted the Ag nanocomposite and Ag-Au nanocomposite on the rat's heart for 3 weeks and measured the biodistribution of Ag ions in the liver, spleen, lung, and kidney using ICP-MS (Fig. 4d). The Au sheath effectively reduces accumulation of Ag ions in all the organs. Histology analysis (Masson's trichrome staining, Hematoxylin and Eosin staining) of the cardiac muscle after 3 weeks of implantation reveals significantly lower fibrotic reaction and inflammatory responses in the Ag-Au nanocomposite than those in the Ag nanocomposite (Fig. 4e, Supplementary Fig. 13a). The data were further analysed by measuring the percentage of fibrotic area over whole area using image-J image analysis software (NIH) and quantitatively confirmed less fibrotic reaction in the Ag-Au nanocomposite compare to the Ag nanocomposite (Supplementary Fig. 13b).

Ag-Au nanocomposite for wearable bioelectronics

Due to the high stretchability and conductivity, we used the Ag-Au nanocomposite to develop wearable bioelectronics for measuring electrophysiological signals and applying electrical/thermal stimulations on the human skin. The Ag-Au nanocomposite and SBS are patterned by using polydimethylsilane (PDMS) molds and assembled (Supplementary Fig. 14a) into a multifunctional wearable electronic patch consisting of recording electrodes to measure electrophysiological signals, bipolar stimulation electrodes, and a heating element to apply electrical and thermal stimulations (Fig. 5a). Because the device is soft and stretchable (Fig. 5b), it can follow the contour of flexible joints such as the wrist (Fig. 5c). The conformal contact minimizes the gap between the electrode and skin, and thus high quality signals can be obtained[30]. Furthermore, the low resistance of the Ag-Au nanocomposite electrodes is helpful to reduce the impedance of the device on the skin (Fig. 5d) and are therefore capable of obtaining electrocardiogram (ECG; from the right forearm with ankle ground) and electromyogram (EMG; from the right forearm) from the human skin with a high signal-to-noise ratio (Fig. 5e).

While electrophysiological signals (*e.g.*, ECG, EMG) provide information on muscle and/or cardiac dysfunction, electrical stimulation is useful for pain relief[31], rehabilitation[32], and prosthetic motor control[33,34]. Therefore, in addition to recording electrophysiological signals, the wearable bioelectronics can be used to concurrently administer therapies through the skin. We applied constant-current monophasic square pulses (Supplementary Fig. 14b) to the skin through the wearable device. Due to lower impedances, the stimulation electrodes made of the Ag-Au nanocomposite have lower threshold current than commercial electrodes, allowing stimulation with high power efficiency (Supplementary Fig. 14c)[35]. The Ag-Au nanocomposite wearable device can simultaneously record EMG signals and deliver electrical stimulations (Fig. 5f). It is well-known that thermal stimulations in conjunction with electrical stimulations can bring synergetic therapeutic effect[14,32]. The stretchable heating element at the centre of the wearable device is used for joule heating. Figure 5g shows the temperature-time profiles with various input voltages. Since the heater shows little resistance change under stretching, heating performance is stable under deformation (Fig. 5h). The softness of the patch ensures firm contact with the skin, allowing reliable heat transfer even when the wrist is flexed or extended (Fig. 5i).

Implantable cardiac bioelectronics using Ag-Au nanocomposite

The Ag-Au nanocomposite is highly conductive, biocompatible, and soft, making them suitable for implantable devices. Various soft cardiac devices (*e.g.*, mesh[11], film[36], and sleeve[37], etc.) have been reported previously on the rat heart model. However, due to intrinsic differences between rodents and human such as the heart rate, cardiac action potential, and pathophysiologic effects of cardiac diseases, studies using large animal models such as the swine model, which accurately approximates the human physiology, are needed[38]. Meanwhile, the large area soft cardiac mesh for recording and stimulating at multiple locations of the swine heart has not been reported yet. Using the Ag-Au nanocomposite, we fabricated a customized large-area cardiac mesh, whose design is based on the detailed shape of the swine heart obtained using magnetic resonance imaging (Fig. 6a). The mesh is designed to cover the entire surface of the ventricles, and it contains multi-channel electrodes for recording and stimulation (Fig. 6b and c).

We simplified the shape of the cardiac silhouette into a conical frustum (Fig. 6b top), which is subsequently unfolded to form a two-dimensional fan shape (Fig. 6c). The cardiac mesh is designed based on this fan shape, which consists of 7 welded repetitive segments, each containing six pairs of electrodes. Each segment is made up of 5 layers: two electrode layers made of the Ag-Au nanocomposite and three insulation layers made of SBS (Fig. 6b bottom and Supplementary Fig. 15a). This multi-layer format enables the multi-channel electrodes to cover from apex to base of the ventricles.

We show that resistance change under mechanical strain is negligible, and the 30% cyclic stretching (considering maximum heart movement[11]) does not change the performance of the cardiac mesh, indicating the implanted mesh is stable during repetitive heart movements (Supplementary Fig. 15b and c). Furthermore, because the modulus of each segment of the cardiac mesh is much lower than the swine myocardium (Supplementary Fig. 15d)[39], the mesh does not interfere with the heart's pumping activity[11,37].

We implanted the cardiac mesh on the swine heart to record myocardial electrophysiology and stimulate the ventricles *in vivo* (Fig. 6d). Figure 6e shows intracardiac electrograms recorded by the multi-channel cardiac mesh that wraps around the ventricles in a healthy swine model. The left anterior descending coronary artery (LAD) was occluded with a balloon catheter to induce acute ischemia mimicking a heart attack in the clinical setting. On the voltage map constructed from the multi-channel mesh recording data, high voltage change in local intracardiac electrograms was observed during ischemia at the anterior wall of the mid-apex left ventricle (Fig. 6f). The surface electrocardiogram and intracardiac electrogram were continuously recorded by limb-leads and the cardiac mesh, respectively. Reliable recording was performed at baseline and during myocardial ischemia, which exhibited clearly differentiated patterns (Fig. 6g). In Fig. 6h, continuous electrical stimulation (*i.e.,* pacing) at different sites produced different QRS configurations in surface ECG with the pacing output of < 1 mA at 2 ms, suggesting adequate compartmentalization of individual electrodes in the cardiac mesh without current leakage or uneven current flow.

Conclusions

In conclusion, we report a new class of highly conductive, biocompatible, and soft nanocomposite using ultralong Ag-Au nanowires and SBS elastomer. Epitaxial deposition of the Au sheath on ultralong Ag nanowires without the galvanic replacement reaction effectively improves biocompatibility by preventing Ag ion leaching and Ag oxidation. High conductivity is attained using ultralong nanowires that formed a high density percolated network in the composite. The ambient solvent drying process during the composite formation along with an optimized content of hexylamine promotes phase separation and formation of a cushy microstructure, generating the soft and highly stretchable nanocomposite. The additional heat rolling-press treatment increases stretchability of the Ag-Au nanocomposite by increasing toughness. When fabricated into a wearable skin-like device and implantable cardiac mesh, the highly conductive Ag-Au nanocomposite follows the contours of a curvilinear human wrist and a pulsating swine heart, allowing electrophysiological signals including surface EMG, surface ECG, and intracardiac electrogram to be monitored, and thermal and electrical stimulations to be administered effectively. These advanced nanocomposite technologies are poised to create new possibilities for next-generation soft bioelectronics.

References

1. Kim, Y., *et al.* Stretchable nanoparticle conductors with self-organized conductive

pathways. *Nature* **500,** 59-63 (2013).

2. Park, M., *et al.* Highly stretchable electric circuits from a composite material of silver nanoparticles and elastomeric fibres. *Nat. Nanotechnol.* **7,** 803-809 (2012).

3. Matsuhisa, N., *et al.* Printable elastic conductors by in situ formation of silver nanoparticles from silver flakes. *Nat. Mater.* **16,** 834-840 (2017).

4. Kim, D. H., *et al.* Epidermal electronics. *Science* **333,** 838-843 (2011).

5. Son, D., *et al.* Multifunctional wearable devices for diagnosis and therapy of movement disorders. *Nat. Nanotechnol.* **9,** 397-404 (2014).

6. Choi, M. K., *et al.* Wearable red-green-blue quantum dot light-emitting diode array using high-resolution intaglio transfer printing. *Nat. Commun.* **6,** 7149 (2015).

7. Lipomi, D. J., *et al.* Skin-like pressure and strain sensors based on transparent elastic films of carbon nanotubes. *Nat. Nanotechnol.* **6,** 788-792 (2011).

8. Miyamoto, A., Lee S., *et al.* Inflammation-free, gas-permeable, lightweight, stretchable on-skin electronics with nanomeshes. *Nat. Nanotechnol.* **12,** 907-913 (2017).

9. You, I., *et al.* Stretchable E-Skin Apexcardiogram Sensor. *Adv. Mater.* **28,** 6359-6364 (2016).

10. Gong S., *et al.* Highly Stretchy Black Gold E-Skin Nanopatches as Highly Sensitive Wearable Biomedical Sensors. *Adv. Electron. Mater.* **1,** 1400063 (2015).

11. Park, J., *et al.* Electromechanical cardioplasty using a wrapped elasto-conductive epicardial mesh. *Sci. Transl. Med.* **8,** 344ra386 (2016).

12. Lu, C., *et al.* Flexible and stretchable nanowire-coated fibers for optoelectronic probing of spinal cord circuits. *Sci. Adv.* **3,** e1600955 (2017).

13. Lee, P., *et al.* Highly stretchable and highly conductive metal electrode by very long

metal nanowire percolation network. *Adv. Mater.* **24,** 3326-3332 (2012).

14. Choi, S., *et al.* Stretchable Heater Using Ligand-Exchanged Silver Nanowire Nanocomposite for Wearable Articular Thermotherapy. *ACS Nano* **9,** 6626-6633 (2015).

15. McShan, D., Ray, P. C., Yu, H. Molecular toxicity mechanism of nanosilver. *J. Food Drug Anal.* **22,** 116-127 (2014).

16. Yang, M., Hood, Z. D., Yang, X., Chi, M., Xia, Y. Facile synthesis of Ag@Au core-sheath nanowires with greatly improved stability against oxidation. *Chem. Commun.* **53,** 1965-1968 (2017).

17. Gong, S., *et al.* A wearable and highly sensitive pressure sensor with ultrathin gold nanowires. *Nat. Commun.* **5,** 3132 (2014).

18. Chen, Y., Ouyang, Z., Gu, M., Cheng, W. Mechanically strong, optically transparent, giant metal superlattice nanomembranes from ultrathin gold nanowires. *Adv. Mater.* **25,** 80-85 (2013).

19. Andres, L. J., *et al.* Rapid synthesis of ultra-long silver nanowires for tailor-made transparent conductive electrodes: proof of concept in organic solar cells. *Nanotechnology* **26,** 265201 (2015).

20. Sun Y., Yin Y., Mayers B. T., Herricks T., Xia Y. Uniform Silver Nanowires Synthesis by Reducing AgNO3with Ethylene Glycol in the Presence of Seeds and Poly(Vinyl Pyrrolidone). *Chem. Mater.* **14,** 4736-4745 (2002).

21. Liu H., Liu T., Zhang L., Han L., Gao C., Yin Y. Etching-Free Epitaxial Growth of Gold on Silver Nanostructures for High Chemical Stability and Plasmonic Activity. *Adv. Funct. Mater.* **25,** 5435-5443 (2015).

22. Yang Y., Liu J., Fu Z. W., Qin D. Galvanic replacement-free deposition of Au on Ag

for core-shell nanocubes with enhanced chemical stability and SERS activity. *J. Am. Chem. Soc.* **136,** 8153-8156 (2014).

23. Dong A., *et al.* A generalized ligand-exchange strategy enabling sequential surface functionalization of colloidal nanocrystals. *J. Am. Chem. Soc.* **133,** 998-1006 (2011).
24. Lee H., *et al.* A graphene-based electrochemical device with thermoresponsive microneedles for diabetes monitoring and therapy. *Nat. Nanotechnol.* **11,** 566-572 (2016).
25. Lee H., Hong Y. J., Baik S., Hyeon T., Kim D. H. Enzyme-Based Glucose Sensor: From Invasive to Wearable Device. *Adv. Healthc. Mater.* (2018).
26. Li J., et al Correlations between Percolation Threshold, Dispersion State, and Aspect Ratio of Carbon Nanotubes. *Adv. Funct. Mater.* **17,** 3207-3215 (2007).
27. Knite, M., Hill, A. J., Pas, S. J., Teteris, V., Zavickis, J. Effects of plasticizer and strain on the percolation threshold in polyisoprene–carbon nanocomposites: Positron annihilation lifetime spectroscopy and electrical resistance measurements. *Mater. Sci. Eng. C* **26,** 771-775 (2006).
28. Sun, J. Y., *et al.* Highly stretchable and tough hydrogels. *Nature* **489,** 133-136 (2012).
29. Dong, J., Abukhdeir, N. M., Goldthorpe, I. A. Simple assembly of long nanowires through substrate stretching. *Nanotechnology* **26,** 485302 (2015).
30. Wang, L.-F., Liu, J.-Q., Yang, B., Yang, C.-S. PDMS-Based Low Cost Flexible Dry Electrode for Long-Term EEG Measurement. *IEEE Sens. J.* **12,** 2898-2904 (2012).
31. Hurley, M. V., Bearne, L. M. Non-exercise physical therapies for musculoskeletal conditions. *Best Pract. Res. Clin. Rheumatol.* **22,** 419-433 (2008).
32. Sarzi-Puttini, P., *et al.* Osteoarthritis: an overview of the disease and its treatment strategies. *Semin. Arthritis Rheum.* **35,** 1-10 (2005).

33. Xu, B., *et al.* An Epidermal Stimulation and Sensing Platform for Sensorimotor Prosthetic Control, Management of Lower Back Exertion, and Electrical Muscle Activation. *Adv. Mater.* **28,** 4462-4471 (2016).

34. Lim, S., *et al.* Transparent and Stretchable Interactive Human Machine Interface Based on Patterned Graphene Heterostructures. *Adv. Funct. Mater.* **25,** 375-383 (2015).

35. Kuiken, T. A., Marasco, P. D., Lock, B. A., Harden, R. N., Dewald, J. P. Redirection of cutaneous sensation from the hand to the chest skin of human amputees with targeted reinnervation. *Proc. Natl. Acad. Sci. U. S. A.* **104,** 20061-20066 (2007).

36. Lee, S., *et al.* A strain-absorbing design for tissue-machine interfaces using a tunable adhesive gel. *Nat. Commun.* **5,** 5898 (2014).

37. Xu, L., *et al.* 3D multifunctional integumentary membranes for spatiotemporal cardiac measurements and stimulation across the entire epicardium. *Nat. Commun.* **5,** 3329 (2014).

38. Lelovas, P. P., Kostomitsopoulos, N. G., Xanthos, T. T. A Comparative Anatomic and Physiologic Overview of the Porcine Heart. *J. Am. Assoc. Lab. Anim. Sci.* **53,** 432-438 (2014).

39. Pham, T., Sun, W. Comparison of biaxial mechanical properties of coronary sinus tissues from porcine, ovine and aged human species. *J. Mech. Behav. Biomed. Mater.* **6,** 21-29 (2012).

Acknowledgement

This work was supported by IBS-R006-D1 and IBS-R006-A1. The authors thank the staff of the National Center for Inter-university Research Facilities (NCIRF) and Research Institute of

Advanced Materials (RIAM) in Seoul National University. We all sincerely thank Dr. Mark Josephson for his material and intellectual support of the animal research.

Author contributions

S.C., S.I.H., D.J., H.J.H., T.H., and D.-H.K. designed the experiments. S.C., S.I.H., D.J., C.L., M.L., H.J.H., T.H., and D.-H.K. performed experiments and analysis. S.C., S.I.H., D.J., H.J.H., C.L., S.B., O.K.P., C.M.T., S.Y.B., S.W.L., K.P., P.M.K., and R.N. performed *in vivo* animal experiments and data analysis. S.I.H., S.W.L., and K.P. performed *in vitro* experiments and analysis. J.W.Y., J.H.R., and W.B.L. performed computer simulation. S.C., S.I.H., D.J., H.J.H., S.B., T.H., and D.-H.K. wrote the paper.

Additional information

Supplementary information is available in the online version of the paper. Reprints and permission information is available online at www.nature.com/reprints. Correspondence and requests for materials should be addressed to T.H. and D.-H. K.

Competing financial interests

The authors declare no competing financial interests.

Figure legends

Figure 1. Fabrication of microstructured Ag-Au nanocomposite. a, Ag-Au nanocomposite is made by combining a mixture of Ag-Au nanowires decorated with hexylamine ligands, SBS elastomer, and an additional hexylamine in toluene. **b**, Illustration of the solvent drying process under ambient conditions. **c**, Schematic showing that the initial solution (left) is separated into a Ag-Au nanowire-rich phase and a SBS-rich phase during dry-casting (middle). Subsequent solvent evaporation (right) forms the microstructured Ag-Au nanowire nanocomposite. (red dot: hexylamine, yellow wire: Ag-Au nanowire, green wire: SBS) **d**, Schematic illustration of the microstructured Ag-Au nanocomposite before and after the stretching. **e**,**f**, Optical camera image of the Ag-Au nanocomposite before (**e**; inset shows before stretching) and after (**f**) the heat rolling-pressed Ag-Au nanocomposite sandwiched between the elastomeric substrates (VHB film). All scale bars, 10 mm.

Figure 2. Characterization and oxidation resistance of Ag-Au nanowire**. a**, SEM image and inset back-scattered electron (BSE) image of Ag-Au nanowires (before surface modification; Au sheath is in yellow). Scale bars, 5 μm and 200 nm (inset). **b**, HRTEM image of the Ag-Au nanowire. Dash line indicates the boundary between Ag core and Au sheath. Inset: an electron diffraction pattern at the Ag-Au boundary showing the crystalline structure of Au in the [111] direction. Scale bar, 5 nm. **c**, EDS elemental mapping of Ag and Au in the bare Ag-Au nanowire, and their merged image confirm the core-sheath structure. Scale bar, 100 nm. **d**, EDS cross-section line scan of the Ag-Au nanowire shows the mean diameter of nanowire is 140 nm and thickness of Au shell is 35 nm. **e**, TEM image of the Ag nanowire (top) and the Ag-Au nanowire (bottom) treated with 1.5 M of H_2O_2. Ag-Au nanowire is protected against oxidation. Scale bars, 100 nm (top) and 200 nm (bottom). **f**, UV-Vis spectra of Ag nanowires (left) and Ag-Au nanowires (right) after H_2O_2 treatment confirm protection of Ag-Au nanowires against oxidation. **g**, Graph shows that nanocomposites with longer Ag-Au nanowires have higher conductivity than those with shorter nanowires. **h**, Graph shows that the nanocomposites with higher Ag-Au nanowire content are more conductive than those with lower Ag-Au nanowire content. Maximum conductivity is 72,700 S/cm at the weight ratio of nanowire:SBS of 75:25 and co-optimized conductivity and stretchability was achieved at the weight ratio of nanowire:SBS of 60:40 where the conductivity is 41,850 S/cm with highest stretchability. **i**, At the same weight ratio of nanowire:SBS of 80:20, conductivity of Ag-Au nanocomposite remains unchanged whereas that of Ag nanocomposite shows a decrease. All error bars represent s.e.m. **j**, SEM image of Ag nanocomposite (top) and Ag-Au nanocomposite (bottom) after 2 hours UV/O_3 treatment. Oxidation is prevented in Ag-Au nanowires. All scale bars, 1 μm.

Figure 3. Effect of phase separation on electrical and mechanical properties. **a**, SEM images of the Ag-Au nanocomposite with hexylamine before (left) and after (right) stretching. Room temperature drying process promotes phase separation and formation of

microstructures with unequal elasticity between the phase separated regions, allowing materials to be stretched. All scale bars, 100 μm. **b**, Stress-strain curve of the Ag-Au nanocomposite with hexylamine for three different solvent drying temperatures. Room temperature (25 ^{o}C) drying lowers Young's modulus and forms a softer composite. **c**, Conductivity change of the Ag-Au nanocomposite under tensile strain for three different drying temperatures. Nanocomposite obtained through room temperature drying is highly conductive and stretchable. **d**, SEM images of the Ag-Au nanocomposite without hexylamine before (left) and after (right) stretching. No microstructures are seen. All scale bars, 100 μm. **e**,**f**, Changes of Young's modulus (**e**) and stretchability (**f**) of the Ag-Au nanocomposite film according to the fraction of hexylamine. Weight ratio of Ag-Au nanowire:SBS is 60:40. All error bars represent s.e.m. **g**,**h**, Map showing stretchability (**g**) and conductivity (**h**) of the nanocomposite at different weight fractions of Ag-Au nanowires, SBS, and hexylamine. The point (0.36:0.24:0.4 weight fraction of Ag-Au nanowires:SBS:hexylamine) indicated by three red dotted lines represents the optimum composition for the highest stretchability. Colour bars in **g**,**f** indicate conductivity (S/cm) and stretchability (%), respectively. **i**, Graphs showing conductivity (left) and stretchability (right) of the Ag-Au nanocomposite at different weigh fractions of hexylamine after the heat rolling-press. The Ag-Au nanocomposite can be stretched up to ~840% when the weight fraction of hexylamine is 0.3. All weight fraction means (each component weight) / (sum of Ag-Au nanowires, SBS, and hexylamine weight). All error bars represent s.e.m. **j**, Graph showing conductivity change of the Ag-Au nanocomposites under tensile strain for the different weight ratios of Ag-Au nanowire and SBS at a fixed weight fraction of hexylamine of 0.3. Inset graph shows the initial conductivity and the conductivity change up to 100% applied strain.

Figure 4. Biocompatibility of Ag-Au nanocomposite *in vitro* and *in vivo*. a, ICP-MS analysis of Ag ions released from Ag nanowires, Ag-Au nanowires, and the Ag-Au nanocomposite after incubating each in DMEM for 3 days. Low levels of Ag ions for Ag-Au nanowires and Ag-Au nanocomposite show that the Au sheath effectively protects Ag nanowires from dissolution. Data are analysed using one-way ANOVA with the Tukey's post hoc test and are expressed as averages ± s.e.m. ($n = 3$). Significance is set at ****$P < 0.0001$ versus the Ag nanowires. **b**, Confocal microscope image of H9C2 cells after exposure to original DMEM (control) or DMEM extracts of Ag nanowires, Ag-Au nanowires, and the Ag-Au nanocomposite for 24 hrs. Cells exposed to Ag nanowire extracts exhibit damaged (arrows) actin cytoskeleton (red) and DNA (blue). Scale bar, 50 μm. **c**, MTT assay shows H9C2, CCD-986sk, and L929 cells exposed to DMEM extracts of Ag nanowires have significantly decreased viability compared to those exposed to original DMEM (control) or extracts of Ag-Au nanowires and Ag-Au nanocomposite. Data are analysed using one-way ANOVA with the Tukey's post hoc test and are expressed as averages ± s.e.m. ($n = 3$). Significance is set at ****$P < 0.0001$ versus the control. **d**, ICP-MS analysis of Ag ions accumulated in liver, spleen, lung, and kidney after sham surgery (control) or implantation of the Ag nanocomposite and the Ag-Au nanocomposite for 3 weeks. Au sheath effectively

reduces Ag ion accumulation in all organs. Data are analysed using one-way ANOVA with the Tukey's post hoc test and are expressed as averages ± s.e.m. (n = 3). Significance is set at *$P < 0.05$ versus the control. **e**, Masson's trichrome staining (left) and hematoxylin & eosin staining (right) of cardiac muscles after 3 weeks implantation of the Ag-Au nanocomposite shows less fibrotic reaction and inflammatory response than those implanted with Ag nanocomposite. Arrows in the first and the third panels indicate fibrosis and inflammatory cells, respectively (n = 5). Scale bars, 250 μm.

Figure 5. Wearable skin-like bioelectronics using the Ag-Au nanocomposite. a, Optical camera image of a multifunctional wearable electronic patch consisting of bipolar stimulation electrodes, electrophysiological signal recording electrodes, and a heating element. Scale bar, 1 cm. **b**,**c**, Optical camera images show the wearable device can be stretched 10%, 50%, and 100% (**b**), making them suitable for flexible joints such as the wrist (**c**). Scale bars, 1 cm and 2 cm for **b** and **c** respectively **d**, Impedance of the Ag-Au nanocomposite electrode at the skin/electrode interface is lower than Ag/AgCl gel electrodes. **e**, Electrocardiogram (ECG) and electromyogram (EMG) measurements obtained through the wearable device on the skin. **f**, EMG signals measured during electrical stimulation. **g**, Temperature profiles of the heating element in the wearable device with applied voltages of 1, 2, and 3 V show reliable heating performance. **h**, Resistance (left axis) and temperature (right axis) change of the heating element under applied strain in longitudinal direction. Inset shows an optical camera image of multifunctional wearable electronic patch stretched in longitudinal direction. **i**, Infrared (IR) camera images show reliable heating performance of the wearable device on a wrist. Colour bar indicates temperature (^{o}C).

Figure 6. Ag-Au nanocomposite-based implantable cardiac mesh for monitoring and stimulating the swine heart *in vivo*. a, 3D cardiac MRI image of a swine heart (red). **b**,**c,** Schematic illustrating the design process for the cardiac mesh. The shape of the heart is simplified as a cone frustum (**b**), which is unfolded into a two-dimensional fan shape (**c**) consisting of 7 repetitive segments welded together. Lower inset in **b** shows the cardiac mesh consists of 2 electrode layers (Ag-Au nanocomposite) and three insulation layers (SBS). **c**,**d**, Optical camera image of a cardiac mesh (**c**) and implanted cardiac mesh on a swine heart (**d**). RV = right ventricle, LV = left ventricle, LAD = left anterior descending coronary artery. Scale bar, 5 cm. **e**, Representative intracardiac electrograms in a healthy swine model (n = 2) recorded by the cardiac mesh, displayed on a 3D reconstructed image of the heart (Red = LV anterior, Orange = LV lateral, Green = LV posterior, and Blue = RV, signals were recorded from 34 electrodes while the other electrodes were connected to the stimulator). **f**, Voltage map is constructed from local intracardiac electrograms recorded by the cardiac mesh during acute ischemia and the anterior wall of the left ventricle shows high voltage change. Acute ischemia is induced by occluding the left anterior descending coronary artery (LAD) using a balloon catheter. **g**, Surface ECG and intracardiac electrograms recorded from healthy and injured regions of the ischemic heart. Arrow indicates ST elevation due to ischemic change.

Following prolonged myocardial ischemia of one hour, ventricular tachycardia occurred. **h**, Representative surface ECG presents different QRS configurations depending on the pacing sites (n = 1). Electrode positions are numbered in **e**.

Methods

Synthesis of Ag-Au nanowires

Growth solution (gold-sulfite complex) is prepared by mixing 1.4 ml of 0.25 M hydrogen tetrachloroaurate(III) hydrate ($HAuCl_4xH_2O$, Strem Chemical Inc., USA), 8.4 ml of 0.2 M sodium hydroxide (NaOH, Sigma Aldrich), 105 ml of 0.01 M sodium sulfite (Na_2SO_3, Sigma Aldrich), and 165 ml of H_2O, and left undisturbed for 12 hrs. A separate solution is prepared by mixing 320 ml of H_2O, 20 ml of Ag nanowires (5 mg/ml), 70 ml of 5 wt% poly-vinylpirrolidone (PVP, M_w 40,000, Sigma Aldrich), 14 ml of 0.5 M sodium hydroxide (NaOH, Sigma Aldrich), 14 ml of 0.5 M L-ascorbic acid (L-AA, Sigma Aldrich), and 3.5 ml of 0.1 M Na_2SO_3. Subsequently, the prepared growth solution was added into the Ag nanowire solution to initiate the reaction and left undisturbed for 2 hrs at the room temperature. Finally, the resulting Ag-Au nanowires were washed multiple times with ethanol and redispersed in dimethylformamide (DMF, Samchun Chemical). For characterization, the SEM image and cross-sectional backscattered electron image of Ag-Au nanowires were obtained by Focused Ion Beam SEM (FIB-SEM, AURIGA, Carl Zeiss, Germany). HRTEM images and energy-dispersive X-ray spectroscopy (EDS) data were obtained by Cs corrected transmission electron microscope (Cs-TEM, JEM-ARM200F, JEOL, Japan).

Preparation of the Ag-Au nanocomposite

The nanocomposite solution is prepared by mixing the SBS polymer solution (10 wt% in toluene), Ag-Au nanowires (30 mg/ml in toluene), and hexylamine with the desired amounts. All weight fraction means (each component weight) / (sum of Ag-Au nanowires, SBS, and hexylamine weight). The solution is dried in a glass mold under desired temperatures. After drying the solution, the Ag-Au nanocomposite is heated under 140 ^{o}C for 5 mins on a hotplate to completely evaporate the remaining solvent. Microscopy images were taken by the field emission scanning electron microscope (FE-SEM, JSM-6701F, JEOL, Japan) and the time of flight secondary ion mass spectrometer (TOF-SIMS, TOF.SIMS-5, ION-TOF, Germany).

Cell viability test

H9C2, CCD-986sk, and L929 are seeded in the 96-well plate with 10,000 cells per well and cultured for 24 hrs. Subsequently, the original DMEM is replaced by extract of samples (control; original DMEM, Ag nanowire, Ag-Au nanowire, and Ag-Au nanocomposite incubated at 37 ^{o}C in DMEM for 10 days) and incubated for another 24 hrs. 20 µl (5 mg/ml) 3-[4,5-dimethylthialzol-2-yl]-2,5-diphenyltetrazolium bromide (MTT) was added to each well and incubated at 37 °C for 4 hrs. Finally, the medium is removed and 200 µl dimethylsulfoxide is added to each well. The absorbance was measured at 540 nm using a 96-well plate reader (Victor X4, Perkin-Elmer, USA).

Cell morphology analysis

H9C2 and CCD-986sk were seeded in the 35 mm glass bottom dish with ~70% confluency and cultured for 24 hrs. Subsequently, the original DMEM was replaced by extract of samples and incubated for another 24 hrs. The cells were fixed with 4 % paraformaldehyde in 1x PBS for 15-20 min and permeabilized with 0.1 % Triton X-100 in 1x PBS for 5 mins. After washing thoroughly with the PBS buffer, cells were incubated with TRITC-conjugated Phalloidin (1:100; Millipore, Billerica, MA, USA) for 50 mins. After washing thoroughly with the PBS buffer, the cells were incubated with DAPI (1:1000; Millipore, Billerica, MA, USA) for 5mins. The morphology of cells was visualized by the confocal microscopy (LSM 780, Carl Zeiss, Oberkochen, Germany).

Histology Analysis

1 cm size serpentine-shape ribbon samples of the Ag nanowire/SBS nanocomposite and the Ag-Au nanowires/SBS nanocomposite were sutured in the rat heart (n = 5). The rats were sacrificed in 3 weeks after the implantation. Harvested organs were fixed with 4% paraformaldehyde in the PBS for 2 days and embedded in paraffin. Each paraffin was sectioned (2 μm) and stained with hematoxylin and eosin (H&E) by following the standard protocol. To visualize collagen fibre deposition in tissues, trichrome staining was performed by using Masson Trichrome Staining Kit (Sigma Aldrich) The histology analysis was made at the region where the suture scar was not present.

Measurement of electrical performance of Ag-Au nanocomposite

The electrical performance was measured using double-layered Ag-Au nanocomposite (15 mm × 3 mm) which was laminated by the heat rolling-press. Conductivity is calculated by the equation[40],

$$\sigma = 1 / \rho_0 \quad (1)$$

$$\rho_0 = \text{film thickness} \times \text{sheet resistance} \quad (2)$$

, where σ is conductivity and ρ_0 is resistivity. The sheet resistance was measured with a custom-made 4-point probe (probe: LS system, Korea; instrument: Keithley 2400, Tektronix, USA), and the thickness was measured by using SEM. For the stretching test, each end of the nanocomposite was connected to a copper wire using the Ag paste and stretched after the encapsulation with VHB films (VHB^{TM} Tape 4910 Clear, 3M, USA). Stretchability and conductivity under strain were measured using two-point-resistance and four-point resistance change, respectively (Keithley 2400, Tektronix, USA). The cyclic performance test was carried out by measuring the two-point resistance while 30% tensile strain was applied repetitively. The resistance was measured using a digital multimeter (NI USB-4065, National Instruments, USA) after releasing the applied strain.

Heat rolling-press of Ag-Au nanocomposite

Two layers of nanocomposite were put in between ketone films and heat rolling-press was applied using a heat roll press (ETK16-486-1, Wellcos Corporation, Korea). Temperature of the rollers was set at 105 ^{o}C. For soft nanocomposite, heat rolling-press was performed until the average thickness was unchanged compared to thickness of the original nanocomposite, while for highly stretchable nanocomposite, the heat rolling-press is performed until the average thickness decrease by 15% compared to thickness of the original nanocomposite. After the process, double-layered nanocomposite was detached from the ketone film. Conductivity and stretchability were measured in the same method as above.

Wearable skin-like bioelectronics using the Ag-Au nanocomposite

The wearable skin-like device was attached to the forearm using Tegaderm (3M, USA), and an Ag/AgCl electrode was placed on the ankle and elbow for ground. The ECG and EMG signals were measured using a data acquisition equipment (DAQ; National Instruments) with the LabVIEW software (encoded with 60 Hz notch filter). The signals were acquired with the sampling rate of 1000 Hz. 3 Hz high-pass filter, 300 Hz low-pass filter, and 59-61 band block filter were applied on the raw data to remove motion artefacts and non-physiological noises. Electrical stimulation was applied through stimulation electrodes. While applying the electrical stimulation, stimulation pulses were measured using EMG electrodes adjacent to the stimulation electrodes. Thermal stimulation was conducted by joule heating. Voltage was applied on the heating element of the wearable skin-like device by the voltage supplier (Agilent, USA). Infrared (IR) camera (Thermovision A320, FLIR system, Sweden) was used for temperature measurement. The impedance at the skin/electrode interface was measured using a pair of Ag/AgCl gel electrodes (2223H Ag/AgCl electrode, 3M, USA) and a pair of Ag-Au nanocomposite films. The Ag-Au nanocomposite was prepared with the size of 1 cm square and attached using the Tegaderm dressing film. The distance between the electrodes was 5 cm. The impedance measurement was conducted using an electrochemical analyser (CHI-660E, CH instruments, Inc., USA). The measurement frequency was scanned from 1 Hz to 90000 Hz. All human experiments were conducted under approval by the Institutional Review Board of the Seoul National University (approval number SNU 17-12-006).

Fabrication of the cardiac mesh

Metal molds with each layer pattern were fabricated. PDMS replicated molds were prepared using the previously-reported fabrication procedure of PDMS mold[13,18]. Prepared nanocomposite solution and SBS solution were patterned on the PDMS mold for electrode layers and encapsulation layers, respectively. Then, the solution is dried under the ambient condition, and the patterned Ag-Au nanocomposite is prepared after solvent is fully evaporated. Each layer is transferred in sequence using PDMS stamp coated with 1:40 (weight ratio of curing agent to prepolymer) ratio of PDMS. For each transfer, the layers were welded under heat of 140 ^{o}C for 20 min. The multi-channel electrodes of the cardiac mesh were connected to a customized flexible printed circuit board using Ag paste, which are, in turn, connected to a ZIF connector on a customized printed circuit board to record signals from each channel and control stimulation sites.

***In vivo* swine experiment**

The research protocol was approved by the Institutional Animal Care and Use Committee and conformed to the Position of the American Heart Association on Research Animal Use. The research was performed at the Beth Israel Deaconess Medical Center, Experimental Electrophysiology Laboratory in Boston, MA. Sedation was initiated with 1.4 mg/kg intramuscular injection of Telazol (tiletamine/zolazepam hydrochloride). Endotracheal intubation was then performed, and general anaesthesia was maintained with isoflurane inhalation (1.5% – 2.5%). Ventilation was maintained between 10 and 16 breaths/min and hemodynamic assessment including heart rate, oxygen saturation, and blood pressure were continuously monitored. After median sternotomy to expose the hearts, the 3D cardiac sock mesh was implanted. Myocardial ischemia was induced by ligation of the mid-left anterior descending artery.

Statistical analyses

Statistical analyses were carried out using the Origin 9.0 software. The one-way ANOVA analysis with the Tukey's post hoc test was used for the Ag ion releasing, cell viability, and biodistribution studies (Fig. 4a, Fig. 4c, and Fig. 4d, respectively). The Shapiro-Wilk test (α = 0.05; n $\geq$ 3 replicates per group) showed that there was no significant deviation from normality. The Levene's test ($\alpha = 0.05$) was performed to all data sets with $n \geq 3$ replicates to test homogeneity of variances. The sample size was selected to ensure adequate power of 90 % for the Ag ion releasing and cell viability studies (Fig. 4a, Fig. 4c, respectively) and 75 % for the biodistribution studies (Fig. 4d). For analysis of percentage of fibrotic area (Supplementary Fig. 13b), the p value was calculated by the Mann-Whitney U-test. The investigators were not blinded to experiments and analyses, and no randomization method was used.

Data availability

The data that support the plots within this paper and other findings of this study are available from the corresponding author upon reasonable request

Reference for Methods

40. Smits F. M. Measurement of Sheet Resistivities with the Four-Point Probe. Bell Syst. Tech. J. 37, 711-718 (1958).

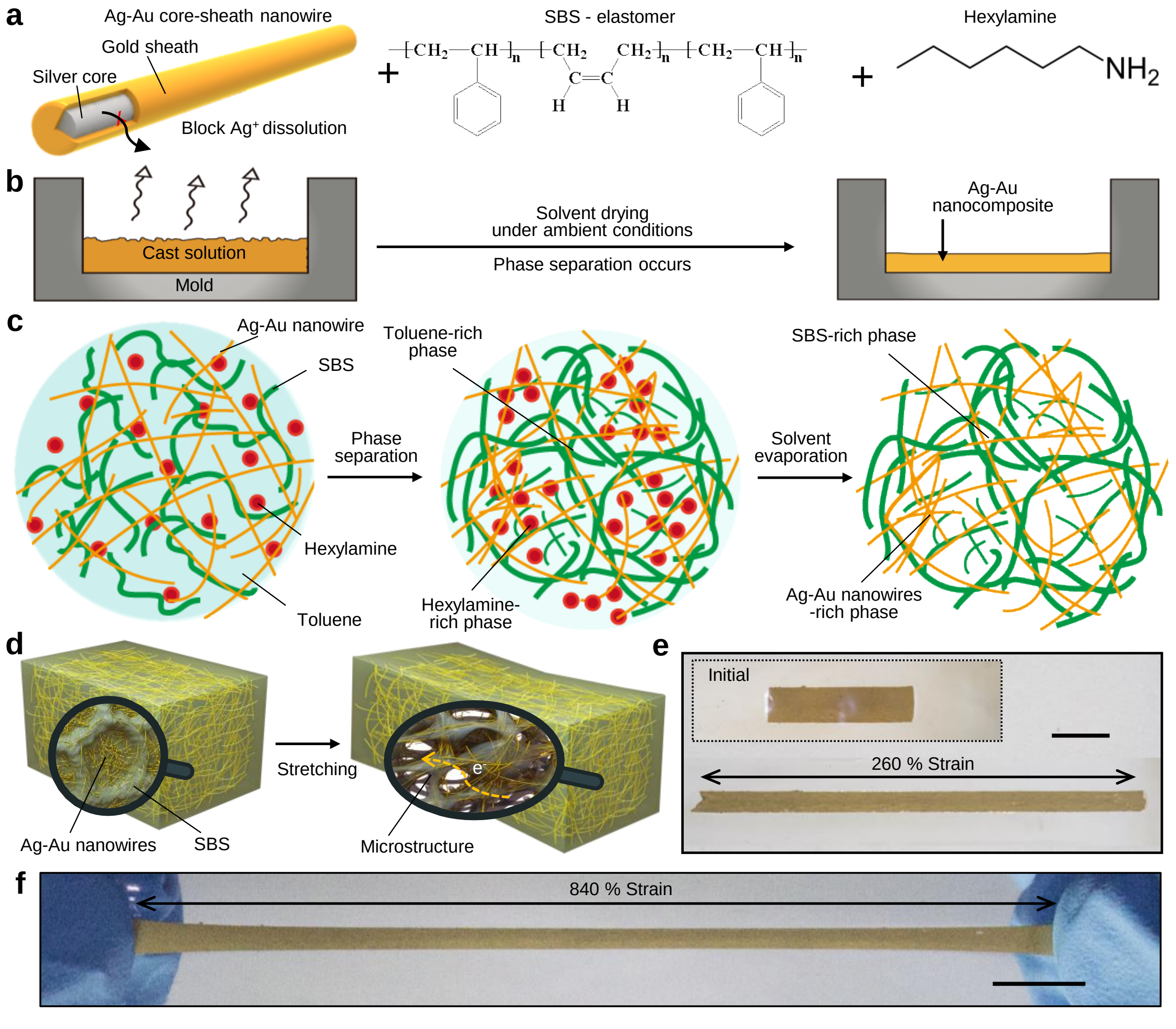

a
Ag-Au core-sheath nanowire
Gold sheath
Silver core
Block Ag+ dissolution
SBS - elastomer
Hexylamine
NH2
b
Cast solution
Mold
Solvent drying
under ambient conditions
Phase separation occurs
Ag-Au
nanocomposite
c
Ag-Au nanowire
SBS
Hexylamine
Toluene
Phase
separation
Toluene-rich
phase
Hexylamine-
rich phase
Solvent
evaporation
SBS-rich phase
Ag-Au nanowires
-rich phase
d
Ag-Au nanowires
SBS
Stretching
Microstructure
e
Initial
260 % Strain
f
840 % Strain

Figure 1

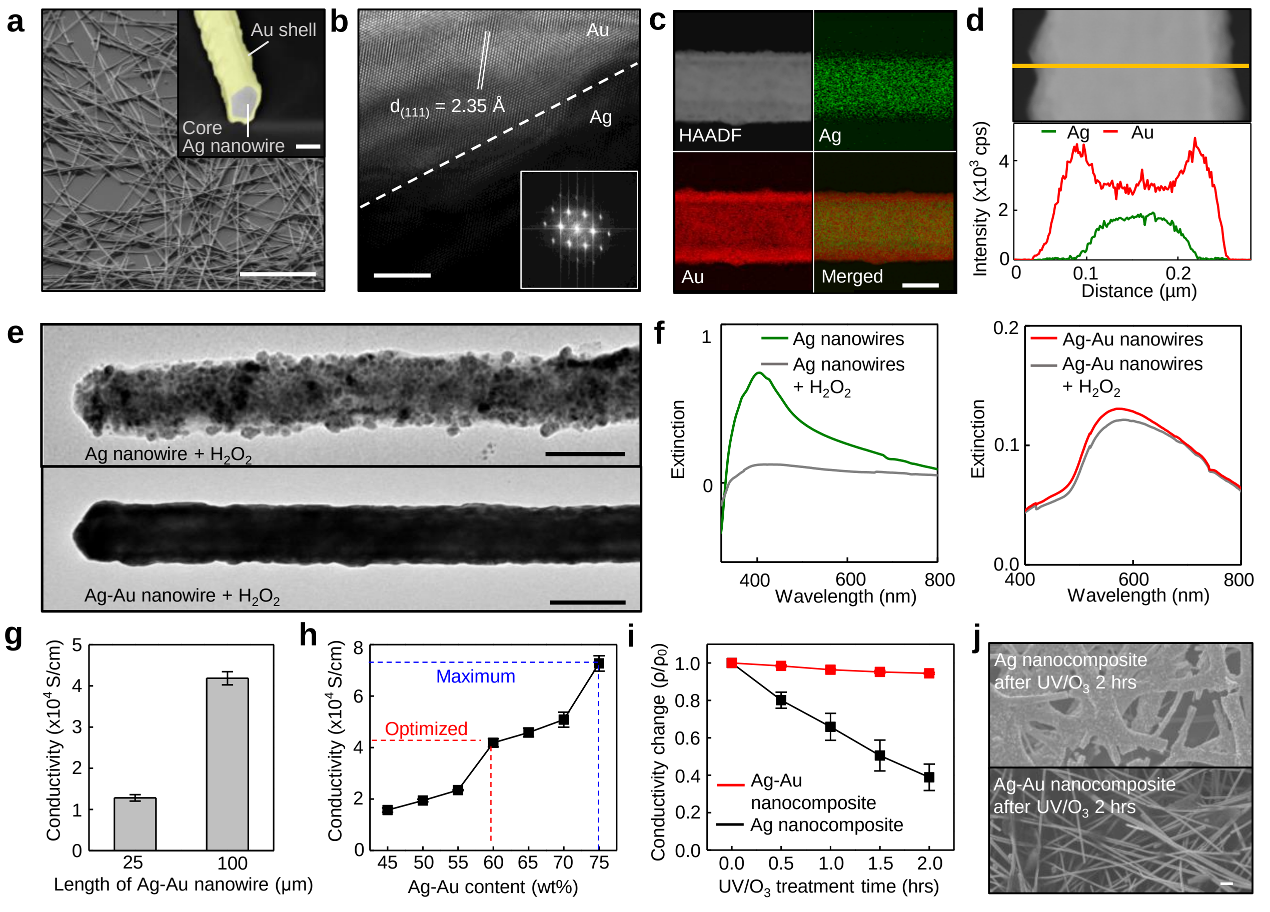

a
Au shell
Core
Ag nanowire
b
Au
d(111) = 2.35 Å
Ag
c
HAADF
Ag
Au
Merged
d
Ag
Au
Intensity (x10^3 cps)
Distance (μm)
e
Ag nanowire + H2O2
Ag-Au nanowire + H2O2
f
Ag nanowires
Ag nanowires + H2O2
Extinction
Wavelength (nm)
Ag-Au nanowires
Ag-Au nanowires + H2O2
g
Conductivity (x10^4 S/cm)
Length of Ag-Au nanowire (μm)
h
Maximum
Optimized
Ag-Au content (wt%)
i
Conductivity change (ρ/ρ0)
Ag-Au nanocomposite
Ag nanocomposite
UV/O3 treatment time (hrs)
j
Ag nanocomposite after UV/O3 2 hrs
Ag-Au nanocomposite after UV/O3 2 hrs

Figure 2

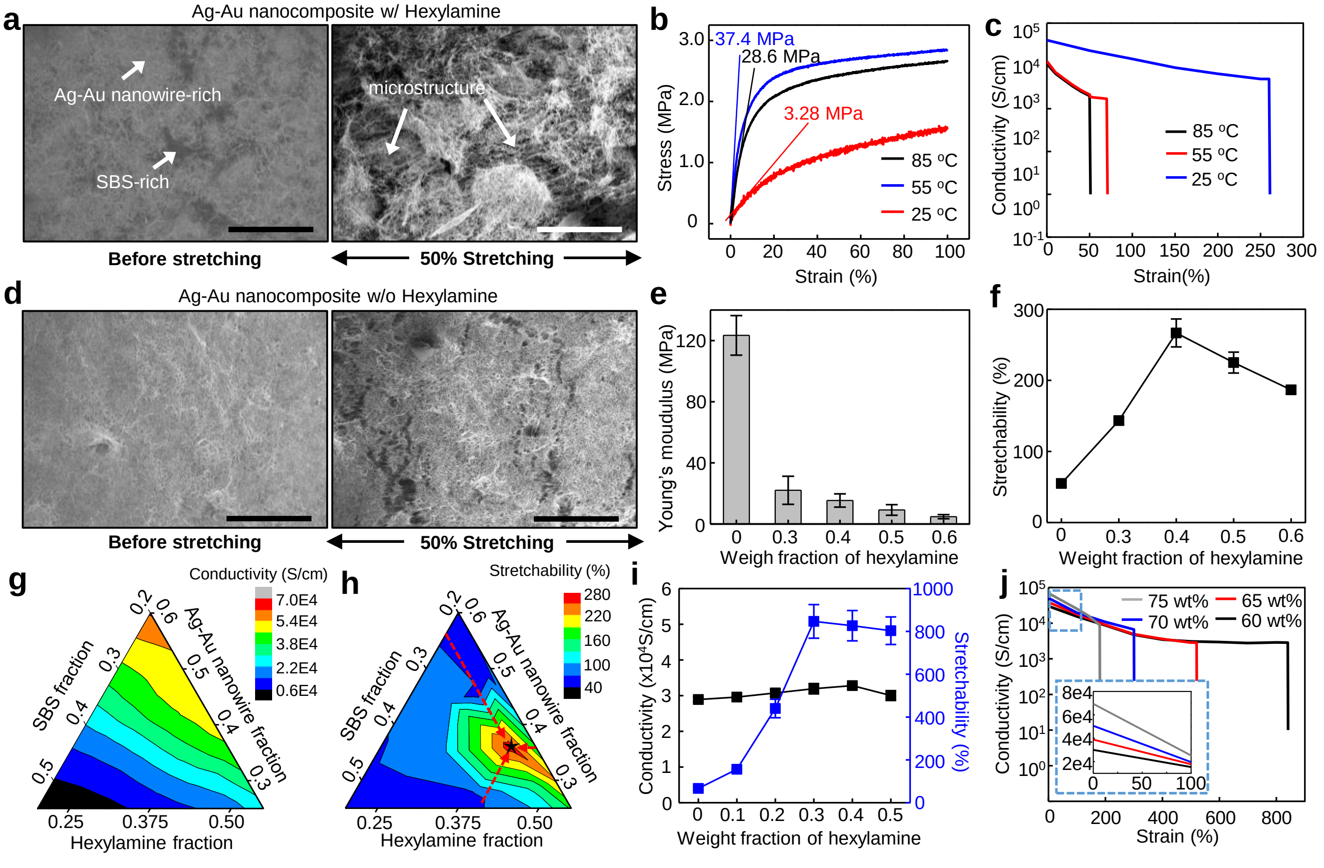

a
Ag-Au nanocomposite w/ Hexylamine
Ag-Au nanowire-rich
SBS-rich
microstructure
Before stretching
50% Stretching
b
37.4 MPa
28.6 MPa
3.28 MPa
85 °C
55 °C
25 °C
Stress (MPa)
Strain (%)
c
Conductivity (S/cm)
Strain(%)
d
Ag-Au nanocomposite w/o Hexylamine
Before stretching
50% Stretching
e
Young's moudulus (MPa)
Weigh fraction of hexylamine
f
Stretchability (%)
Weight fraction of hexylamine
g
Conductivity (S/cm)
7.0E4
5.4E4
3.8E4
2.2E4
0.6E4
SBS fraction
Ag-Au nanowire fraction
Hexylamine fraction
h
Stretchability (%)
280
220
160
100
40
SBS fraction
Ag-Au nanowire fraction
Hexylamine fraction
i
Conductivity (x10⁴S/cm)
Stretchability (%)
Weight fraction of hexylamine
j
75 wt%
65 wt%
70 wt%
60 wt%
Conductivity (S/cm)
Strain (%)

Figure 3

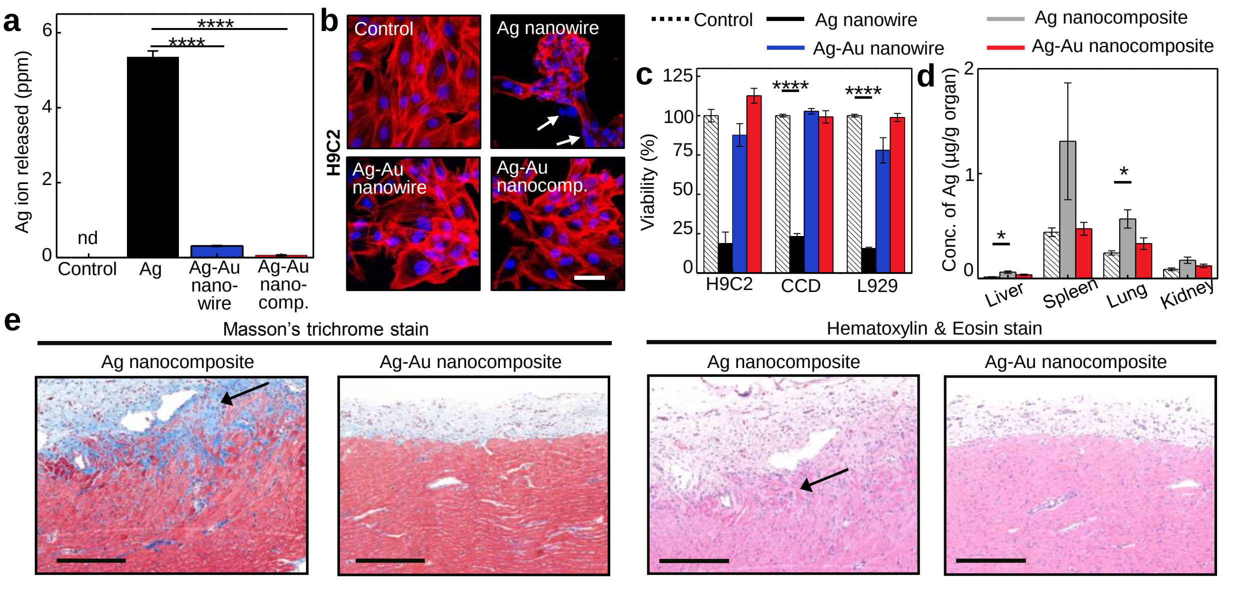

a
Ag ion released (ppm)
0
2
4
6
nd
****
****
Control
Ag
Ag-Au nano-wire
Ag-Au nano-comp.
b
H9C2
Control
Ag nanowire
Ag-Au nanowire
Ag-Au nanocomp.
Control
Ag nanowire
Ag-Au nanowire
Ag nanocomposite
Ag-Au nanocomposite
c
Viability (%)
0
25
50
75
100
125
****
****
H9C2
CCD
L929
d
Conc. of Ag (μg/g organ)
0
1
2
*
*
Liver
Spleen
Lung
Kidney
e
Masson's trichrome stain
Hematoxylin & Eosin stain
Ag nanocomposite
Ag-Au nanocomposite
Ag nanocomposite
Ag-Au nanocomposite

Figure 4

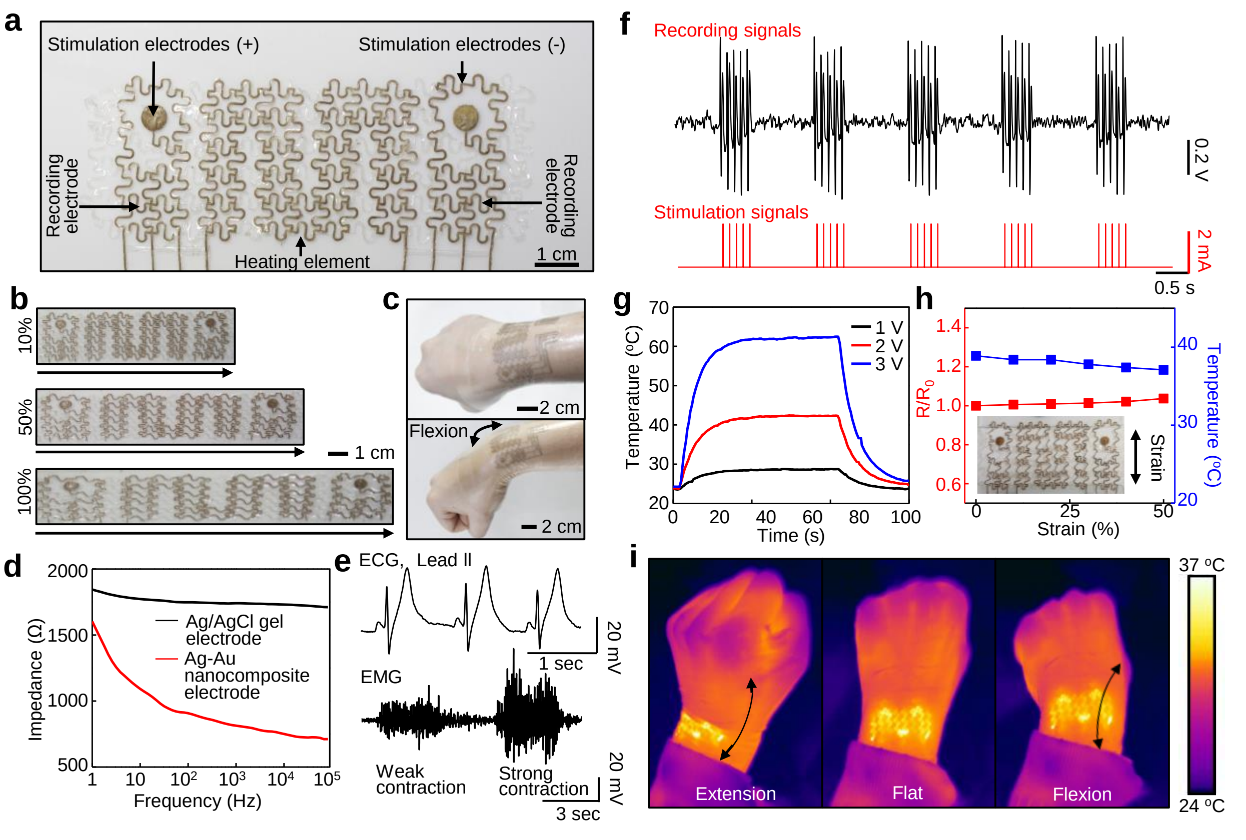
a
Stimulation electrodes (+)
Stimulation electrodes (-)
Recording electrode
Recording electrode
Heating element
1 cm
b
10%
50%
100%
1 cm
c
2 cm
Flexion
2 cm
d
Impedance (Ω)
Frequency (Hz)
Ag/AgCl gel electrode
Ag-Au nanocomposite electrode
e
ECG, Lead II
1 sec
20 mV
EMG
Weak contraction
Strong contraction
3 sec
20 mV
f
Recording signals
0.2 V
Stimulation signals
2 mA
0.5 s
g
Temperature (°C)
Time (s)
1 V
2 V
3 V
h
R/R0
Temperature (°C)
Strain (%)
Strain
i
Extension
Flat
Flexion
37 °C
24 °C

Figure 5

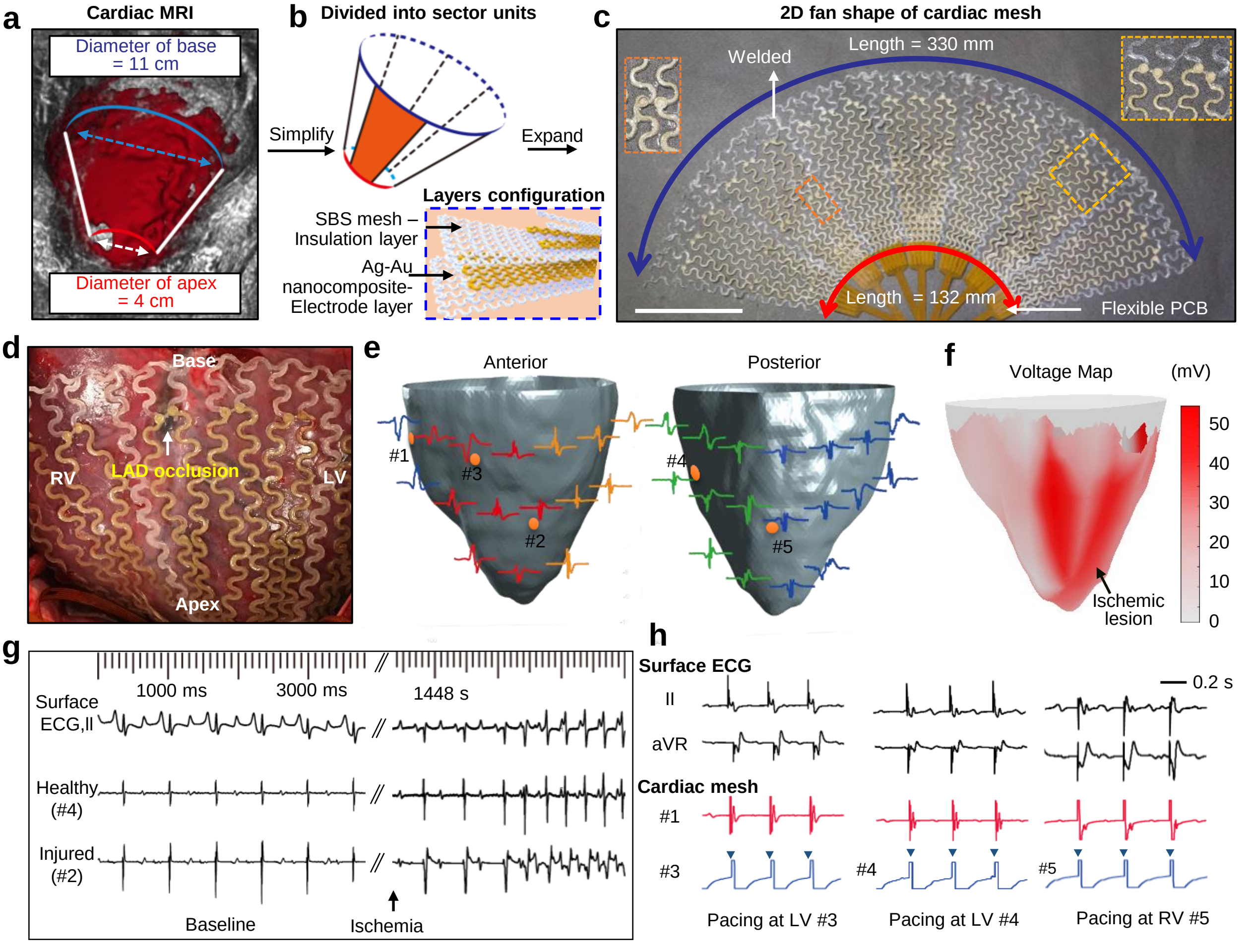

a
Cardiac MRI
Diameter of base = 11 cm
Diameter of apex = 4 cm
b
Divided into sector units
Simplify
Expand
Layers configuration
SBS mesh – Insulation layer
Ag-Au nanocomposite- Electrode layer
c
2D fan shape of cardiac mesh
Welded
Length = 330 mm
Length = 132 mm
Flexible PCB
d
Base
RV
LAD occlusion
LV
Apex
e
Anterior
Posterior
#1
#3
#2
#4
#5
f
Voltage Map
(mV)
50
40
30
20
10
0
Ischemic lesion
g
1000 ms
3000 ms
1448 s
Surface ECG,II
Healthy (#4)
Injured (#2)
Baseline
Ischemia
h
Surface ECG
0.2 s
II
aVR
Cardiac mesh
#1
#3
#4
#5
Pacing at LV #3
Pacing at LV #4
Pacing at RV #5

Figure 6